

SNARE-Mediated Fusion of Single Chromaffin Granules with Pore-Spanning Membranes

Raphael Hubrich,¹ Yongsoo Park,^{2,3} Ingo Mey,¹ Reinhard Jahn,² and Claudia Steinem^{1,4,*}

¹Institute of Organic and Biomolecular Chemistry, University of Göttingen, Göttingen, Germany; ²Max-Planck Institute for Biophysical Chemistry, Göttingen, Germany; ³Department of Molecular Biology and Genetics, Koc University, Sarıyer, Istanbul, Turkey; and ⁴Max-Planck Institute for Dynamics and Self-Organization, Göttingen, Germany

ABSTRACT Pore-spanning membranes (PSMs) composed of supported membrane parts as well as freestanding membrane parts are shown to be very versatile to investigate SNARE-mediated fusion on the single-particle level. They provide a planar geometry readily accessible by confocal fluorescence microscopy, which enabled us for the first time, to our knowledge, to investigate the fusion of individual natural secretory granules (i.e., chromaffin granules (CGs)) on the single-particle level by two-color fluorescence microscopy in a time-resolved manner. The t-SNARE acceptor complex Δ N49 was reconstituted into PSMs containing 2 mol % 1,2-dipalmitoyl-*sn*-glycero-3-phosphatidylinositol-4,5-bisphosphate and Atto488-1,2-dipalmitoyl-*sn*-glycero-3-phosphoethanolamine, and CGs were fluorescently labeled with 2-((1*E*,3*E*)-5-((*Z*)-3,3-dimethyl-1-octadecylindolin-2-ylidene)penta-1,3-dien-1-yl)-3,3-dimethyl-1-octadecyl-3*H*-indol-1-ium perchlorate. We compared the dynamics of docked and hemifused CGs as well as their fusion efficacy and kinetics with the results obtained for synthetic synaptobrevin 2-doped vesicles fusing with PSMs of the same composition. Whereas the synthetic vesicles were fully immobile on supported PSMs, docked as well as hemifused CGs were mobile on both PSM parts, which suggests that this system resembles more closely the natural situation. The fusion process of CGs proceeded through three-dimensional post-lipid-mixing structures, which were readily resolved on the gold-covered pore rims of the PSMs and which are discussed in the context of intermediate states observed in live cells.

INTRODUCTION

Soluble N-ethylmaleimide-sensitive factor attachment receptor (SNARE) proteins are not only the engines for neuronal exocytosis but are also key players in most of the fusion processes in the secretory pathway of eukaryotic cells (1,2). In neuroendocrine cells such as chromaffin cells, SNAREs are essential for the release of hormones and neuroactive peptides into the bloodstream by catalyzing the exocytosis of large dense-core vesicles — the chromaffin granules (CGs) (3). CGs utilize the same basic fusion machinery as synaptic vesicles. In both systems, the major fusogenic components are the SNARE proteins syntaxin 1A, SNAP25, and synaptobrevin 2 (4–7). Reconstitution of this fusion machinery in artificial membranes has been key in understanding the molecular details of SNARE-mediated fusion. In particular, single-vesicle fusion assays are well suited. They are superior over bulk fusion assays because they allow distinguishing

different fusion intermediates, and kinetic aspects, such as docking lifetimes, can be quantified (8–11). Over the years, several setups have been evolved that are well suited for single-vesicle fusion studies. On the one hand, planar-supported lipid bilayers with reconstituted proteins have been developed (9,10,12–15). On the other hand, highly curved proteoliposomes have been immobilized on the surface (16–19). Both membrane systems allow measuring fusion of SNARE-doped unilamellar vesicles on the single-particle level by means of fluorescence microscopy. Although the majority of studies focused on the minimal fusion machinery (i.e., recombinantly expressed and purified proteins), only very few studies combined a SNARE reconstituted synthetic membrane with natural vesicles like CGs (4,6,20). CGs harbor the machinery required for fusion (7) that, in contrast to synthetic vesicles, is embedded in a complex and crowded natural membrane environment, which can alter the fusion behavior considerably. So far, two different synthetic membrane systems have been reported: 1) Recently, Jahn and co-worker (4) used giant unilamellar vesicles (GUVs) for the fusion of CGs. However, the three-dimensional structure of a GUV makes it

Submitted July 26, 2018, and accepted for publication November 29, 2018.

*Correspondence: csteine@gwdg.de

Editor: Arne Gericke.

<https://doi.org/10.1016/j.bpj.2018.11.3138>

© 2018 Biophysical Society.

Hubrich et al.

very difficult to track a CG, particularly as the docked and fusing vesicle rapidly diffuses on the slightly curved GUV membrane. 2) Tamm and co-workers (6,20) used solid supported membranes (SSMs) providing a planar geometry, which is readily accessible by fluorescence microscopy. The SSMs contained the SNARE acceptor complex composed of syntaxin 1A and SNAP25 (1:1) with which CG fusion events were monitored using content release. A disadvantage of this in vitro assay is the fact that the CGs were immediately immobile after docking to the SSM. In live chromaffin cells, however, a very diverse diffusion behavior is observed for CGs adjacent to the plasma membrane (21–23). The finding of different mobility states in live cells led to the classification of the vesicles into pools of primed and docked CGs (24,25). Another aspect that has been recently discussed for CGs in live chromaffin cells is intermediate fusion states. By super-resolution fluorescence microscopy, Wu and co-workers (26) investigated the mechanism of CG fusion and found a sequential transition from intact vesicle to hemifusion and then to full fusion. The fusion-generated Ω -profiles were highly dynamic and may enlarge or shrink (27).

To overcome the drawback of fully immobile docked vesicles and to observe possible intermediate fusion states by fluorescence microscopy in a time-resolved manner, we used planar pore-spanning membranes (PSMs) (28,29). These membranes consist of freestanding PSM (f-PSM) and supported PSM (s-PSM) areas and thus allow a comparison of the diffusive and fusion behavior of docked vesicles on the two different membrane types under otherwise exact same conditions. Recently, Kuhlmann et al. (30) showed that synthetic vesicles doped with synaptobrevin 2 are mobile if they are docked to f-PSMs but immobile if docked to s-PSMs. s-PSMs further allowed them to observe intermediate fusion states. In this study, we took advantage of these features of PSMs to investigate the diffusive behavior as well as the fusogenicity of single CGs isolated from the adrenal medulla of bovine glands and to compare the results with those obtained for synthetic vesicles under otherwise same conditions.

MATERIALS AND METHODS

Materials

Porous SiO₂/Si₃N₄ substrates were received from Aquamarijn Micro Filtration (Zutphen, the Netherlands). 1,2-Dioleoyl-*sn*-glycero-3-phosphocholine (DOPC), 1-palmitoyl-2-oleoyl-*sn*-glycero-3-phospho-L-serine (POPS), and 1-palmitoyl-2-oleoyl-*sn*-glycero-3-phosphoethanolamine (POPE) were from Avanti Polar Lipids (Alabaster, AL). Texas Red 1,2-dipalmitoyl-*sn*-glycero-3-phosphoethanolamine triethylammonium salt (TexasRed-DPPE), cholesterol, and 6-mercapto-1-hexanol (6-MH) were purchased from Sigma Aldrich (Taufkirchen, Germany), whereas Atto488-1,2-dipalmitoyl-*sn*-glycero-3-phosphoethanolamine (Atto488-DPPE) was acquired from Atto-tec (Siegen, Germany). 1,2-dipalmitoyl-*sn*-glycero-3-phosphatidylinositol-4,5-bisphosphate (PIP₂) was purchased from MoBiTec (Göttingen, Germany), and 2-((1E,3E)-5-((Z)-3,3-dimethyl-1-octadecylindolin-2-ylidene)penta-1,3-dien-

1-yl)-3,3-dimethyl-1-octadecyl-3H-indol-1-ium perchlorate (DiD-C₁₈) was purchased from Thermo Fisher Scientific (Waltham, MA).

Protein expression and isolation

Recombinant expression of the SNARE syntaxin 1A (amino acids [aa] 183–288), SNAP25a (aa 1–206 with all cysteines replaced by serine), and the two fragments of synaptobrevin 2 (aa 49–96 and aa 1–96) was carried out in transformed *Escherichia coli* BL21(DE3) cells containing a pET28a vector with the respective DNA sequence. All SNAREs, originating from *Rattus norvegicus*, were equipped with a His₆ tag for the first step of purification via Ni²⁺-NTA agarose affinity chromatography. Subsequently, the His₆ tags were cleaved by thrombin followed by ion-exchange chromatography on MonoQ or MonoS columns (ÄKTA purifying system; GE Healthcare, Little Chalfont, UK). The t-SNARE complex Δ N49 was assembled from syntaxin 1A, SNAP25a, and synaptobrevin 2 (aa 49–96) and purified by ion-exchange chromatography on a MonoQ column in the presence of 3-[(3-cholamidopropyl)dimethylammonio]-1-propanesulfonate (1% (w/v)) as described previously (30,31).

Δ N49 reconstitution into vesicles

The comicellization method in the presence of *n*-octyl- β -D-glycoside (*n*-OG) and a subsequent detergent removal by size-exclusion chromatography was applied to reconstitute the Δ N49 complex into vesicles as described previously (31,32). Briefly, lipids (DOPC/POPE/POPS/PIP₂/cholesterol/Atto488-DPPE; 48:19:10:2:20:1 (*n/n*); 0.5 mg total) were mixed from stock solutions and dried under a stream of nitrogen followed by further solvent removal in vacuum for 2 h at 30°C. The lipid films were solubilized in 50- μ L buffer (20 mM HEPES, 100 mM KCl, 1 mM dithiothreitol, 0.1 mM EGTA (pH 7.4)) supplemented with *n*-OG. Δ N49 solution was added, which resulted in a final concentration of 75 mM *n*-OG and a protein/lipid ratio (p/l) of 1:500. The mixed micelle solution was incubated for 30 min at 0°C followed by size-exclusion chromatography (illustra NAP-10 G25 column; GE Healthcare) in buffer to remove detergent. Subsequently, a second size-exclusion step in ultrapure water was performed to remove residual detergent and salts. The proteoliposome suspension was dried on indium tin oxide coated glass slides in a desiccator over a saturated sodium chloride solution (relative humidity 80%) to form multibilayer stacks, which were transformed into GUVs by electroformation (3 h; 1.6 V_{peak-to-peak}; 12 Hz) in 200 mM sucrose solution. For control experiments, Δ N49 solution was incubated with an excess of the soluble SNARE domain of synaptobrevin 2 (aa 1–96) before the reconstitution into GUVs.

Preparation of PSMs

Porous SiO₂/Si₃N₄ substrates were rinsed with ethanol, dried under a stream of nitrogen, and then treated by argon plasma (30 s; Zepto plasma cleaner; Diener Electronic, Ebhausen, Germany). The cleaned surface was sputter coated (25 s; 40 mA; 0.08 mbar; Cressington sputter coater 108auto; Elektronen-Optik-Service, Dortmund, Germany) with a thin titanium layer followed by deposition of a 30-nm-thick gold layer by thermal evaporation under high vacuum (Med 020; Bal-Tec, Balzers, Liechtenstein). The gold-coated porous substrates were incubated overnight at 4°C in a 1-mM *n*-propanolic solution of 6-MH resulting in a hydrophilic 6-MH self-assembled monolayer. For PSM preparation, the hydrophilically functionalized substrates were thoroughly rinsed with ethanol and buffer and placed in a buffer-filled chamber immediately followed by an addition of proteo-GUV suspension (5–10 μ L) directly onto the substrate. After incubation for 30 min at room temperature, the chamber was carefully rinsed with buffer to remove GUVs that did not spread, and PSM formation was monitored by confocal fluorescence microscopy.

CG purification and labeling

CGs were isolated from the adrenal medulla of bovine glands using a continuous sucrose gradient for final purification as described in Park et al. (7). Purified CGs were labeled by incubation with the lipophilic dye DiD-C₁₈ (2.5 μ M; 1 h at room temperature). Excess of DiD-C₁₈ was removed by dialysis (2.5 h at 4°C).

Fluorescence microscopy

Fluorescence images were taken with an upright confocal laser scanning microscope (Zeiss Laser Scanning Microscope 710; Zeiss, Jena, Germany) equipped with a water immersion objective (W Plan-Apochromat; 63 \times ; numerical aperture = 1.0; Zeiss). A 488-nm argon laser was used to excite the Atto488-DPPE doped PSMs, whereas the DiD-C₁₈ labeled CGs were excited with a 633-nm helium neon laser. Emission light was spectrally separated and collected by photomultiplier tubes in ranges of 495–545 nm for Atto488-DPPE and 640–729 nm for DiD-C₁₈.

Detection of single CG fusion events and data analysis

Single CG fusion events with PSMs were monitored in time series of 2500 frames with a time resolution of 122 ms/frame and an image resolution of 256 \times 256 square pixels related to an area of $\sim 40 \times 40 \mu\text{m}^2$ at room temperature. The identification of CG docking and fusion on PSMs was evaluated manually. Time-resolved fluorescence intensity traces were extracted by placing a 4 \times 4 square pixel region of interest (ROI) on the center of mass of each detected CG followed by the readout of the average intensity in this ROI in all frames of the time series. Mobile CGs were tracked with the software TrackNTrace (33) by fitting the point spread function to the intensity profile of the CG, which allowed detection of displacements with subpixel resolution. The tracking data were used to guide the ROI for the intensity readout. Further, the mean-square displacement (MSD) was calculated from the trajectories by the histogram method implemented in TrackNTrace (33). The histograms followed a Gaussian function, and each one was fitted accordingly to obtain σ^2 . Diffusion coefficients were determined by fitting a linear regression to the MSD versus time interval plot to the first 4–13 data points. The CG pore-center distance analysis was performed as described in the [Supporting Materials and Methods](#).

RESULTS AND DISCUSSION

Single CG fusion events with PSMs

To investigate single events of SNARE-mediated fusion of natural dense-core secretory granules (i.e., CGs) with artificial PSMs, we reconstituted the t-SNARE acceptor

complex Δ N49 (initial p/l of 1:500) consisting of syntaxin 1A, SNAP25a, and a stabilizing fragment of synaptobrevin 2 (aa 49–69) into the PSM. PSMs were composed of DOPC/POPE/POPS/PIP₂/cholesterol (48:20:10:2:20, *n/n*) and doped with 1 mol % Atto488-DPPE for fluorescence imaging. DiD-C₁₈-labeled CGs naturally containing the v-SNARE synaptobrevin 2 (5,34) were added to the PSMs, and their docking and fusion were investigated by dual-color confocal laser scanning fluorescence microscopy.

Fig. 1 shows the setup along with a fluorescence micrograph of a Δ N49-doped PSM, to which fluorescently labeled CGs have been added. The PSMs on the pores (f-PSMs) are visible as green areas, whereas the PSMs on the pore rims (s-PSMs) appear black because of the quenching of the fluorescence on the gold-covered surface (35–37). Several CGs, visible as red and green spots, are discernible in the plane of the PSMs, indicating an interaction between the CGs and the PSM (Videos S1 and S2). To prove that the observed interaction between CGs and PSMs is SNARE specific, a control experiment was performed in which the Δ N49 complex was blocked with the v-SNARE fragment synaptobrevin 2 (aa 1–96) before reconstitution, resulting in PSMs with inactive t-SNARE complexes. In this experiment, no docking of the CGs to the PSMs was observed, confirming SNARE specificity (Video S3).

We tracked each fluorescently labeled CG docked onto the PSM and obtained characteristic time traces for the red and green fluorescence intensities as shown in Fig. 3. The observed time traces of the two fluorescence channels can be rationalized as shown in Fig. 2, which schematically depicts the proposed scenario of docking and fusion of CGs with s-PSMs (Fig. 2, top) and the corresponding expected theoretical fluorescence time traces of the green and the red channel (Fig. 2, bottom). Every fusion event starts with docking of the CG to the PSM (i) marked by a sharp increase of the red fluorescence intensity (DiD-C₁₈), whereas the green fluorescence intensity (Atto488-DPPE) remains unaffected. We refer to this situation as “pre-lipid-mixing” state; at this state, the CG appears red in the fluorescence micrographs. At the onset of fusion between the CG and the PSM (ii), the lipids and therefore the fluorescent markers of the PSM and the CG start

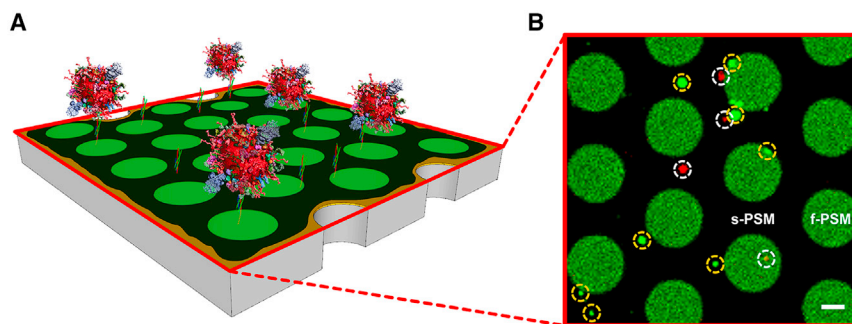


FIGURE 1 (A) A schematic three-dimensional illustration of a PSM patch fluorescently labeled with Atto488-DPPE (green) and doped with the t-SNARE complex Δ N49. DiD-C₁₈-labeled CGs docked to the PSM are depicted in red (not drawn to scale). (B) Shown is a fluorescence micrograph of a PSM patch with docked CGs (highlighted in dashed white circles) on both membrane areas (i.e., the supported PSM (s-PSM) and freestanding PSM (f-PSM) parts) as well as fused CGs (highlighted in dashed yellow circles) appearing green because of influx of the PSM-marker Atto488-DPPE into the CG membrane upon fusion; scale bars, 2 μ m. To see this figure in color, go online.

Hubrich et al.

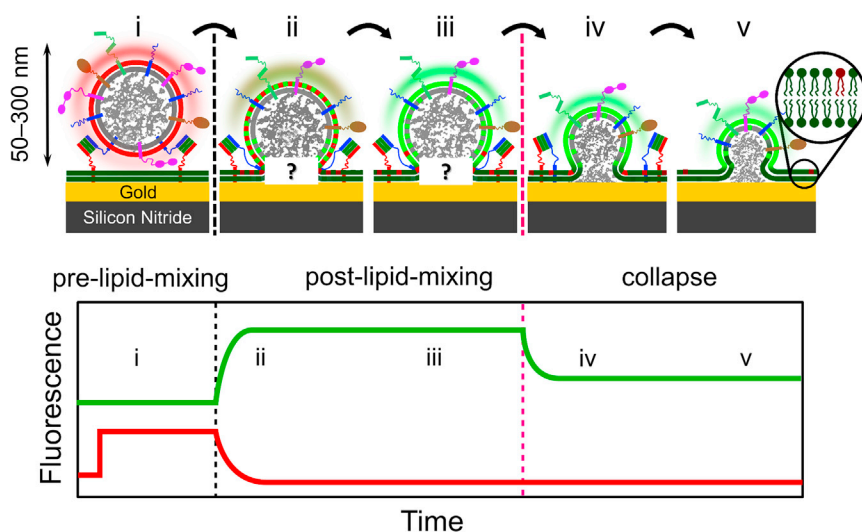


FIGURE 2 (Top) A schematic illustration of the process of CG docking and fusion and (bottom) the corresponding fluorescent time traces of a CG docking and fusion event on an s-PSM. The event starts with a DiD-C₁₈-labeled CG docked to an Atto488-DPPE-doped PSM (i). At this stage, the CG appears red. Upon fusion, DiD-C₁₈ diffuses out of the CG membrane into the PSM and is quenched, while Atto488-DPPE simultaneously diffuses into the CG membrane and is dequenched (ii and iii). At this stage, the CG appears green and remains in a three-dimensional structure, which might be attributed to a hemifusion state or a transient opening and closing fusion pore. However, from the pure lipid labeling, it cannot be distinguished between hemifusion and fusion pore formation (see “?” in ii and iii, top). The subsequent decrease in the green fluorescence intensity is caused by a collapse of the three-dimensional CG post-lipid-mixing structure into the planar PSM (iv and v). To see this figure in color, go online.

mixing. Mixing leads to a decrease in red fluorescence intensity because of the diffusion of DiD-C₁₈ into the PSM where it is quenched by the underlying gold layer. Simultaneously, the PSM marker Atto488-DPPE diffuses into the CG membrane until saturation is reached (iii) and is dequenched because of the increased distance of Atto488-DPPE to the gold layer. We refer to this situation as “post-lipid-mixing” state. The collapse of the three-dimensional structure upon merging of the CG membrane into the PSM results in a decrease in the green fluorescence intensity (iv and v) as the green fluorophores come closer to the gold layer, and thus, quenching by the gold layer is observed (37–39). This collapse can be interpreted as full

fusion of both membrane leaflets leading to a shrinkage of the CG post-lipid-mixing structure.

Although all evaluated fluorescence time traces exhibit this general signature of docking and fusion, they differ in the longevity of the post-lipid-mixing structure. To account for this observation, we classified the process of CG docking and fusion into three types (Fig. 3, A–C). The three classes mainly differ in the time when the three-dimensional CG post-lipid-mixing structure starts collapsing into the PSM.

Fig. 3 A shows a time trace in which the CG does not collapse into the PSM until the end of the time series (i.e., the CG remains as a green three-dimensional structure on the s-PSM). At this stage, a hemifusion intermediate state

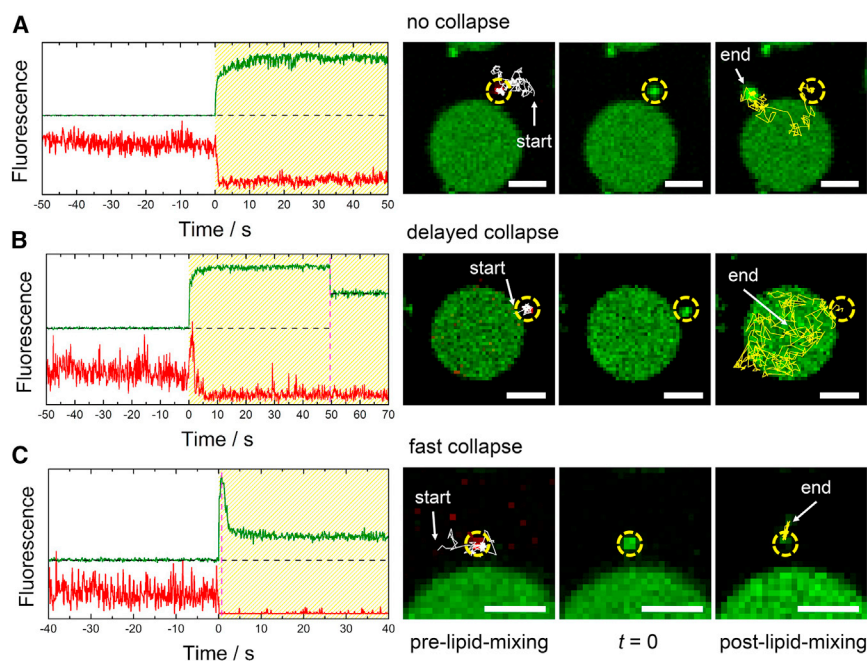


FIGURE 3 (Left) Time-resolved fluorescence intensity traces of DiD-C₁₈-marked CGs (red) upon docking and fusing with Atto488-DPPE-labeled PSMs (green) doped with the ΔN49 complex. The time period of post-lipid-mixing is shaded in yellow. The magenta dotted lines mark the time points of CG collapse. The black dotted lines mark the fluorescence intensities of the baselines. Of note, in (B), two different baselines are given, one referring to the s-PSM and the other one to the f-PSM at which the CG has fused. (Right) Fluorescence micrographs of the corresponding intensity curves showing the last frame before the onset of lipid mixing (pre-lipid-mixing), the frame when lipid mixing starts ($t = 0$), and the last frame of the time series (post-lipid-mixing) are shown. The diffusion trajectories of the CGs before (white) and after (yellow) lipid mixing are depicted as solid lines. The position of the CG is highlighted with a dashed circle; scale bars, 2 μm . (A) A fusion event with a stable three-dimensional post-lipid-mixing structure is shown. (B) A fusion event with a delayed collapse of the CG is shown. (C) A fusion event with a fast collapse of the CG is shown. To see this figure in color, go online.

could be assumed or a transient opening and closing of a fusion pore. However, because only the lipid membrane of the CG is labeled, we cannot distinguish between hemifusion and fusion pore formation. Fig. 3 B shows an example of a delayed collapse. The CG docks at the s-PSM and turns into the post-lipid-mixing state on the s-PSM. It diffuses into the f-PSM area at which it eventually collapses. Because the s-PSM and f-PSM have different green fluorescence intensities, the baselines of the s-PSM and f-PSM differ (see Fig. 3 B, black dotted lines). The time trace shown in Fig. 3 C is a result of a fast collapse (within ~ 600 ms) after the onset of lipid mixing on the s-PSM in which a small green three-dimensional structure remains.

We found that only on f-PSMs, a full collapse of CGs was observed, which means that the green fluorescence intensity decreased to the baseline level of the f-PSM. Such full collapse of a CG is similar to what has been reported by Witkowska and Jahn (4), who also observed full fusion events of CGs with freestanding GUV membranes. However, full collapse of a CG in the f-PSM occurred only in $\sim 1\%$ of the detected events. In 99% of the events, a three-dimensional CG post-lipid-mixing structure resulting in a green fluorescence intensity that is larger than the baseline level was observed on s-PSMs. This observation indicates that an intermediate state such as a hemifused state or a transient pore opening and closing arrests the CG in the post-lipid-mixing structure. Owing to the attachment of the PSM to the support, it is well conceivable that the crowded CG membranes cannot readily merge into the s-PSMs and remain in a three-dimensional structure and that the dense-core CG content, mainly composed of neuroactive peptides and proteins, cannot be released quickly into the thin water layer between the bilayer and the substrate, respectively.

For a statistical analysis, we recorded 20 time series from four independent experiments and detected and evaluated 290 CG fusion events. 170 (59%) of these events exhibited a stable three-dimensional structure after the onset of lipid mixing that did not collapse until the end of the recorded time series as shown in Fig. 2 A. 100 (34%) of the detected CG fusion events showed a delayed collapse (Fig. 2 B), whereas in the remaining 20 (7%) CG fusion events, the three-dimensional CG structure collapsed immediately after the onset of lipid mixing (Fig. 2 C). For comparison of the statistics, we performed fusion experiments with synthetic vesicles composed of DOPC/POPE/POPS/cholesterol/TexasRed-DPPE (50:19:10:20:1) and doped with synaptobrevin 2 (p/1 1:500) on PSMs with the same composition used for CG fusion (Fig. S2 A). Compared to synthetic vesicles fusing with s-PSMs in which $\sim 90\%$ of the docked vesicles hemifuse or fully fuse into PSMs that contain 2 mol % PIP₂, only 41% of the CGs in the post-lipid-mixing state proceed to fusion. That means that $\sim 60\%$ of the CGs remain in a noncollapsed state. This cannot be explained solely by the fluidity of the s-PSM or possible defects in the membrane because the PSMs used

for synthetic vesicle and CG fusion experiments were identical. It is more likely that the protein-crowded membrane and the dense content of the CGs prevent them to fully merge into the PSM. Our comparison with synthetic vesicles thus shows that the artificial system possibly neglects the impact of membrane crowding on the fusion process.

Three-dimensional post-fusion structures of CGs in live cell chromaffin cells have been described previously. Wu and co-workers (26,27) investigated modes of CG exo- and endocytosis in live chromaffin cells using confocal and stimulated emission depletion microscopy. They found hemifused states as well as dynamic Ω -shaped CG postfusion structures merging slowly or rapidly with the plasma membrane of chromaffin cells. Based on their results, they developed a model for the fusion-generated Ω -profiles referred to as Ω -exo-endocytosis and suggested to redefine the fusion modes of “kiss & run” and “full collapse” as rapid and slow closures of the Ω -shaped profile (27).

Kinetics of single CG fusion events

The advantage of the two-color fluorescence readout and the fact that the CGs appear green in the post-lipid-mixing state allowed us to gather information about the lifetime of the docking state (τ_{docking}) of the CGs as well as the lifetime of the CG postfusion structures before the onset of collapse (τ_{3D}). Time-resolved fluorescence intensity traces of an exemplary single CG fusion event that capture these two observables are depicted in Fig. 4 A. The accuracy of τ_{docking} depends on the overall labeling of the CG and is defined as the time difference between the time point of the increased red fluorescence intensity and the time point at which the green fluorescence intensity increases. τ_{3D} is given as the time difference between the time point at which the green fluorescence intensity increases and the time point at which it starts decreasing again.

For a statistical analysis, we determined the docking lifetimes of 104 CGs bound to the PSMs, which were cast into a histogram (Fig. 4 B). A general model proposed by Floyd et al. (40,41) was employed to shed some light on the CG fusion kinetics and to compare the results with previous ones (31) and those obtained with synthetic vesicles fused with PIP₂-doped PSMs as described below. In this model, the rate-limiting step from docking to the onset of fusion is not defined as a one-step transition but as a series of N hidden transitions with a single rate constant k_1 for each transition (Eq. 1) as follows:

$$pdf(\tau_{\text{docking}}) = \frac{k_1^N \times \tau_{\text{docking}}^{N-1}}{\Gamma(N)} \times \exp(-k_1 \times \tau_{\text{docking}}), \quad (1)$$

with $\Gamma(N)$ being the γ function. By fitting Eq. 1 to the dwell-time distribution of docked CGs, a rate constant of $k_1 = 0.040 \pm 0.004 \text{ s}^{-1}$ with $N = 3.2 \pm 0.3$ was determined.

Hubrich et al.

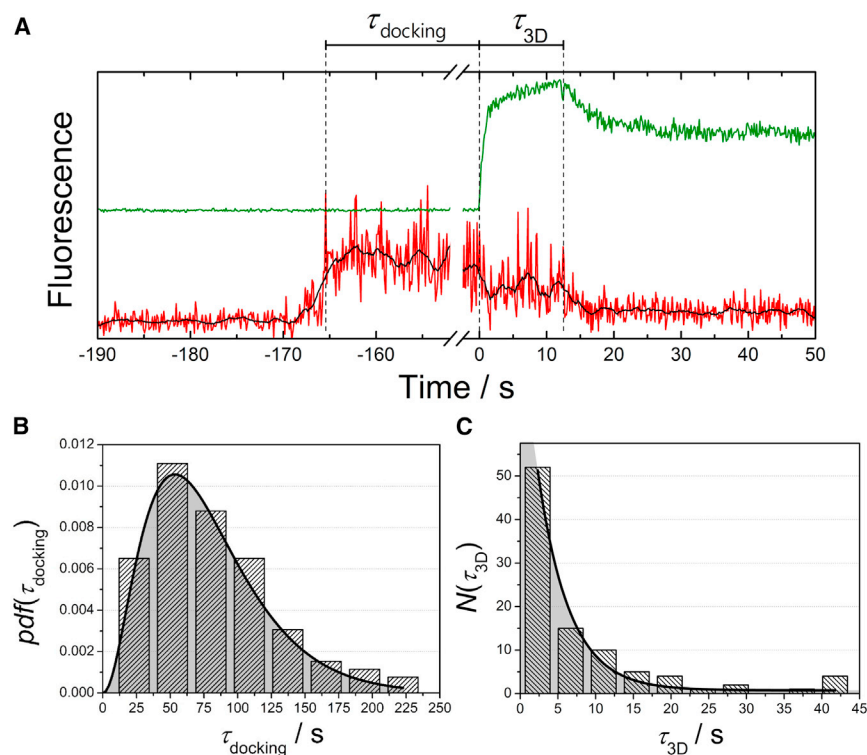


FIGURE 4 (A) Exemplary time-resolved fluorescence intensity traces of a single CG fusion event that shows the observables of interest—the lifetime of the docking state (τ_{docking}) and the lifetime of the three-dimensional structure before the onset of collapse (τ_{3D}). (B) Histogram of lifetimes of the docking state τ_{docking} . The black line is the result of fitting Eq. 1 to the data. (C) Histogram of determined values for τ_{3D} of a total number of 98 CG fusion events on PSMs with reconstituted $\Delta N49$ complex. Fitting of a mono-exponential decay (Eq. 2) to the data results in a rate constant for the CG post-lipid-mixing structure starting to collapse into the PSM of $k_2 = 0.24 \pm 0.05 \text{ s}^{-1}$ and thus an average lifetime of the intact three-dimensional structure of $4.2 \pm 0.9 \text{ s}$. To see this figure in color, go online.

This leads to an average docking lifetime of a CG on a $\Delta N49$ -doped PSM of $\bar{\tau}_{\text{docking}} = k_1^{-1} \times N = 80 \pm 16 \text{ s}$. This determined docking lifetime is much larger than that observed for the fusion of CGs with GUVs (4) but is on the same order of magnitude as docking lifetimes of synthetic vesicles with PSMs (31).

For a direct comparison, we measured the docking lifetime as well as the lifetime of the intermediate states of synthetic vesicles composed of DOPC/POPE/POPS/cholesterol/TexasRed-DPPE (50:19:10:20:1) and doped with synaptobrevin 2 (p/l 1:500) on PSMs with the same composition used for CG fusion (Fig. S2 B). We found a docking lifetime of $\bar{\tau}_{\text{docking}} = 61 \pm 5 \text{ s}$. The difference in docking lifetime between synthetic vesicles and CGs is minor, with a trend for the CGs to stay longer in the docked state as the synthetic vesicles, which can be attributed to the much larger protein content of the CG membranes (5). The protein shell of the CG alters the contact of the CG membrane with the PSM upon SNARE complex formation.

To evaluate the stability of three-dimensional CG post-lipid-mixing structures, values for τ_{3D} were extracted from intensity traces of 98 single CG fusion events and cast into a histogram (Fig. 4 C). To determine k_2 , the rate constant for the onset of the collapse of the three-dimensional structure into the PSM, Eq. 2 was fit to the histogram as follows:

$$N(\tau_{3D}) = N_0 \times \exp(-k_2 \times \tau_{3D}), \quad (2)$$

with N_0 being the total number of instable CG post-lipid-mixing structures. k_2 was determined to be 0.24 ± 0.05

s^{-1} , which means that the average lifetime of the three-dimensional structure before the onset of collapse is $k_2^{-1} = 4.2 \pm 0.9 \text{ s}$. A semistable intermediate fusion state was also found for synthetic vesicle fusion on PSMs (Fig. S2 C), showing a similar distribution of intermediate fusion lifetimes as monitored for CGs. In both cases, synthetic vesicle as well as CG fusion, a mono-exponential decay (Eq. 2) with similar rate constants k_2 fitted the data best, suggesting a consistent one-step mechanism for the decay of the intermediate fusion state. These results indicate that the actual fusion process proceeds in both cases via intermediate states and that the lifetimes of the states are not significantly influenced by the membrane composition (i.e., the protein content) of the fusing vesicles.

Diffusion behavior of CGs on PSMs

A characteristic feature of CGs bound to PSMs that is not observed if synthetic SNARE-doped vesicles are bound to s-PSMs (30) is that CGs are mobile on both parts of the PSM, that is, on both the f-PSM and s-PSM parts (Videos S4 and S5).

Moreover, mobility was observed not only in the pre-lipid-mixing state (Video S4, red colored CGs) but also after the onset of lipid mixing (i.e., in the post-lipid-mixing state (Video S5, green colored CGs)).

Fig. 5 shows the trajectories of a CG in the pre-lipid-mixing state (Fig. 5 A) and in the post-lipid-mixing state (Fig. 5 B) demonstrating that CGs are able to cross the pore

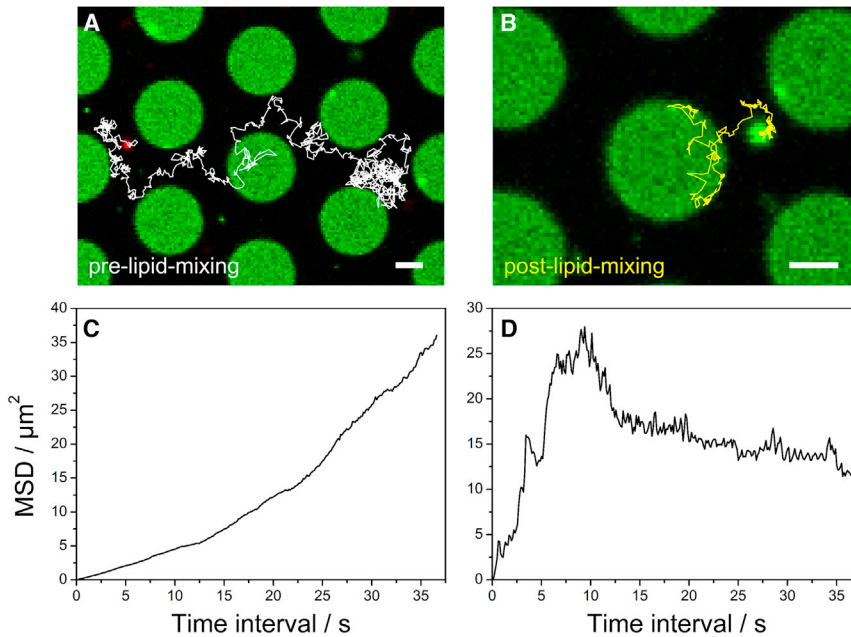


FIGURE 5 Fluorescence micrographs of the last frame of a time series showing CG diffusion on PSMs across pore boundaries (A) before and (B) after the onset of lipid mixing. Diffusion trajectories are depicted as white or yellow lines, respectively; scale bars, 2 μm . Mean-square displacement (MSD) of the CG as a function of time intervals corresponding to the CG diffusion is shown for (C) pre-lipid-mixing and (D) post-lipid-mixing. To see this figure in color, go online.

boundaries. This is in contrast to what has been observed for synthetic SNARE-doped vesicles, which were immediately immobile upon docking to s-PSMs and mobile but trapped within the pores while docking to f-PSMs (30). To verify that this observation is not a function of the lipid composition of the PSM, we performed experiments with PSMs composed of DOPC/POPE/POPS/cholesterol/PIP₂/Atto488-DPPE (48:19:10:20:2:1) and doped with the $\Delta\text{N}49$ complex (p/l 1:500) to which vesicles composed of DOPC/POPE/POPS/cholesterol/TexasRed-DPPE (50:19:10:20:1) and doped with synaptobrevin 2 (p/l 1:500) were added. For all detected vesicles, those docked on s-PSMs were immobile (Fig. S3).

From the trajectories, we computed the MSD. On short time intervals of several hundred milliseconds, CG diffusion was found to be unhindered, resulting in a linear correlation of the MSD versus time intervals with a slope of $4D$, from which the diffusion constant of each individual CG was calculated (Fig. S4). Individual trajectories of diffusing CGs only dwelling either on the f-PSMs or the s-PSMs before (pre-lipid-mixing (pre-lm)) or after (post-lipid-mixing (post-lm)) the onset of fusion was analyzed to yield average diffusion coefficients on the distinct membrane areas (Fig. 6). Diffusion coefficients on the f-PSM were determined to be $\bar{D}_{\text{f-PSM}}$ (pre-lm) = $0.34 \pm 0.06 \mu\text{m}^2/\text{s}$ and $\bar{D}_{\text{f-PSM}}$ (post-lm) = $0.40 \pm 0.13 \mu\text{m}^2/\text{s}$. For comparison, diffusion coefficients of synthetic vesicles on f-PSMs are only slightly smaller with average diffusion coefficients of $\bar{D}_{\text{f-PSM}}$ (pre-lm) = $0.24 \pm 0.01 \mu\text{m}^2/\text{s}$ and $\bar{D}_{\text{f-PSM}}$ (post-lm) = $0.27 \pm 0.02 \mu\text{m}^2/\text{s}$. Apparently, CG diffusion is not altered by the fusion state (i.e., whether the particle is in the pre-lipid-mixing state or post-lipid-mixing state on f-PSMs). On s-PSMs, mean diffusion coefficients for CGs

are smaller by trend with $\bar{D}_{\text{s-PSM}}$ (pre-lm) = $0.12 \pm 0.05 \mu\text{m}^2/\text{s}$ and $\bar{D}_{\text{s-PSM}}$ (post-lm) = $0.04 \pm 0.03 \mu\text{m}^2/\text{s}$.

Previously, we have discussed that the immobility of the $\Delta\text{N}49$ complex might be the reason why synthetic synaptobrevin 2-doped vesicles docked to the $\Delta\text{N}49$ complex reconstituted in s-PSMs are immobile (30). However, in contrast to synthetic synaptobrevin 2-doped vesicles, CGs are not fully immobile on s-PSMs, which implies that it is more likely that besides the diffusive behavior of the $\Delta\text{N}49$ complexes in the PSM, frictional coupling of the vesicle is responsible for the observed diffusion (42). Frictional coupling is expected to be reduced for CGs compared to synthetic vesicles owing to the large protein content in the

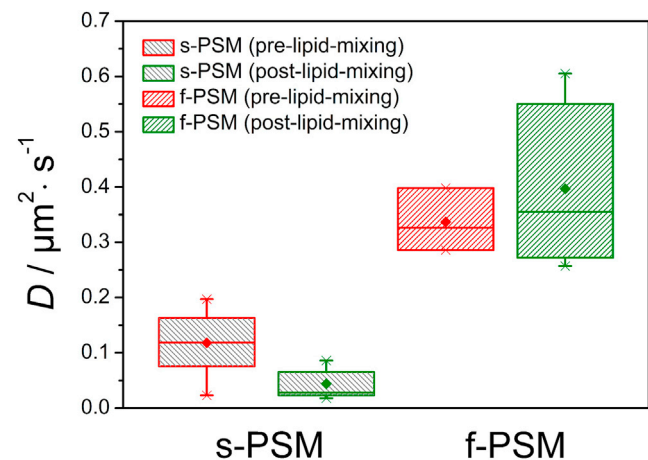


FIGURE 6 A boxplot of MSD-derived diffusion coefficients D of SNARE-bound CGs on $\Delta\text{N}49$ -doped PSMs before and after the onset of lipid mixing. For diffusion analysis, CG diffusion trajectories either on s-PSMs or f-PSMs were taken. To see this figure in color, go online.

Hubrich et al.

membrane, which can serve as a spacer between vesicle and planar membrane. Frictional coupling is particularly apparent on s-PSMs. CGs couple more strongly to the s-PSM than to the f-PSM, particularly in the post-lipid-mixing state, showing that the support impacts the interaction between CG and planar membrane significantly because of the van der Waals attraction of the substrate.

To our knowledge, PSMs constitute the first planar chip-based model membrane on which full mobility of CGs is observed. In single CG fusion experiments, recently conducted by Tamm and co-workers (6,43) on SSMs, CGs were immediately immobile after docking. Because CG mobility was found in various *in vivo* studies to be an important characteristic to draw conclusions on their fusion state (docked or primed) or the fusion mode (kiss & run or full collapse) (21–23,25,44), the model system of PSMs in combination with properly labeled CGs might provide additional information about the fusion states in the future. For example, Nofal et al. (25) stained CGs by overexpressing neuropeptide Y fused to monomeric red fluorescent protein and observed the diffusion behavior of single CGs in live chromaffin cells. CG mobility was visualized by total internal reflection fluorescence microscopy. With this method, they were able to identify three different types of CG mobility, namely, immobility, restricted caged mobility, and free or directed mobility. They assigned these three different types of motion to the distinct pools of primed CGs, docked CGs, and CGs in depot, respectively. Similarly, Henry and co-workers (24) focused on the analysis of secretory vesicle motion in human carcinoid BON cells. Also, for this different kind of secretory vesicles and cell line, a very similar diffusion behavior was observed by total internal reflection fluorescence microscopy. The monitored diffusion trajectories of the secretory vesicles showed a very diverse and transient behavior and were subdivided into the motion states of stalled, constrained, free, and directed diffusion (24). However, *in vivo*, the diffusion coefficients of the particles were by one to two orders of magnitude lower ($(2.07 \pm 0.06) \times 10^{-3} \mu\text{m}^2/\text{s}$ (45); $(2.2 \pm 0.8) \times 10^{-3} \mu\text{m}^2/\text{s}$ (24)) than those observed for CGs on PSMs, which might be attributed to the cytoskeleton (21) and the larger viscosity of the cytosol.

To analyze the motion states of CGs on PSMs, we performed a detailed analysis of the trajectories as a function of the position of the CG on the membrane in the pre-lipid-mixing state and post-lipid-mixing state. The PSM is a membrane with two different areas (s-PSMs and f-PSMs), in which the membrane components diffuse differently (30,31). Moreover, at the boundary of s-PSM and f-PSM, the membrane is locally bent (29). It is conceivable that the topography of the PSM also influences the diffusion behavior. We distinguished all positions on f-PSMs and s-PSMs taking the geometry of the pore array into account (Fig. 7, A and B). The pore center is set to zero, and all CG diffusion trajectories were analyzed with regard to their

distance r_x to the nearest pore center with the pore radius r_{pore} . For pre-lipid-mixing CG diffusion, 218 diffusion trajectories from 8 different time series were evaluated. In case of post-lipid-mixing CG diffusion, 45 trajectories from 9 different time series were analyzed. From the qualitative inspection of the trajectories, we conclude that CGs (pre-lipid- and post-lipid-mixing state) stay confined for a certain time period on s-PSMs and at the edges of the pores before they continue to diffuse, whereas they diffuse freely on f-PSMs, which is also reflected in the histograms showing the number counts of positions of the CGs (Fig. S5). The normalized histograms taking the geometric areas into account (Fig. 7, C and D, top panels; Fig. S7) show the same for the pre- and post-lipid-mixing state. The probability density is large on the s-PSM and at the border of the pores. This result indicates that the fusion state (pre-lipid-mixing and post-lipid-mixing state) does not significantly influence the diffusion behavior of CGs, but rather, the support impacts CG mobility as a result of the enhanced frictional coupling. Another aspect is possible defects in the supported membrane parts that prevent the particle from moving, which do not occur in f-PSMs and which cannot be ruled out in membranes attached to a support. Moreover, the topography of the PSM, which is bent at the border ($r_x/r_{\text{pore}} = 1$) between s-PSM and f-PSM (46) further enhances the conformal contact of the particle with the membrane, and thus, the tendency to stay fixed at these positions is even more pronounced.

To have a closer look at CGs exhibiting a certain mobility state, two different displacement filters were applied (Fig. S6). All CG positions were excluded that resulted in a jumping distance (JD) of either $<0.05 \mu\text{m}^2/\text{s}$ or $<0.20 \mu\text{m}^2/\text{s}$ (Fig. 7, C and D, middle and bottom panels). The fraction of the different CG mobility states in the pre-lipid-mixing and post-lipid-mixing state are compiled in Table 1. Although CGs in the pre-lipid-mixing state are found equally distributed in the three (arbitrarily set) mobility states, CGs in the post-lipid-mixing state are primarily found in the least mobile state, which is in agreement with our previous finding that CGs in the post-lipid-mixing state couple more strongly to the s-PSM owing to the underlying substrate. These results suggest that the different mobility states found in living cells might be a result of the intermediate state of the CG but also how strongly the particle is frictionally coupled to the membrane.

CONCLUSIONS

PSMs are a versatile tool to measure SNARE-mediated single-vesicle fusion events by means of fluorescence microscopy on a quasiplanar membrane geometry allowing for a high spatial and time resolution. Our results demonstrate that CGs isolated from the adrenal medulla of bovine glands behave significantly different from synthetic vesicles with respect to their diffusive behavior as well as their postfusion

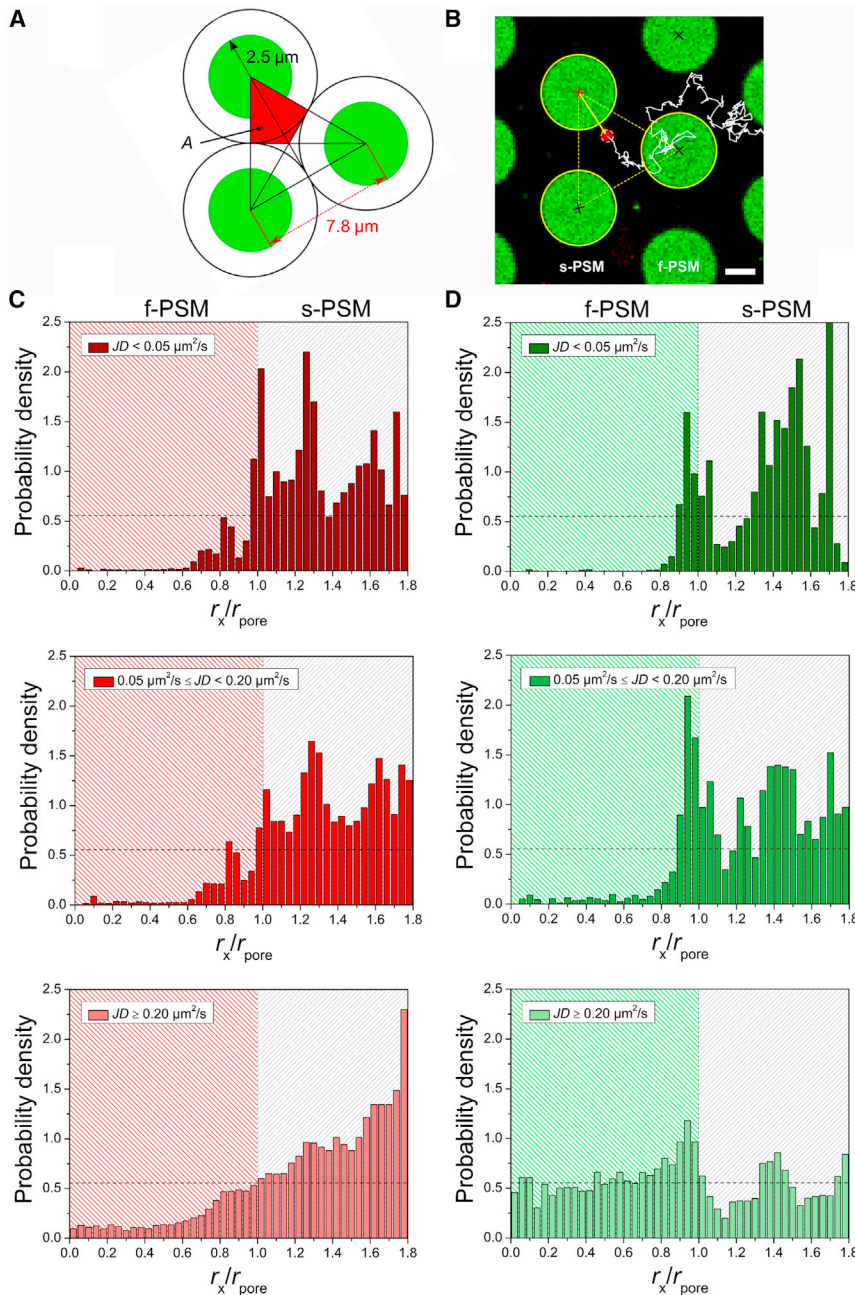


FIGURE 7 (A) A schematic illustration of the triangular unit cell used for CG-pore-center distance determinations ($r_{\text{pore}} = 2.5 \mu\text{m}$; pore-to-pore distance = $7.8 \mu\text{m}$). 1/3 of the unit cell, corresponding to the catchment area A of one pore center in this unit cell, is depicted in red. (B) A fluorescence micrograph of a CG (red) diffusing on a PSM (green) with the diffusion trajectory depicted as a white line and the relevant unit cell as a dashed, yellow triangle is shown. The pore center with the shortest distance to the CG is highlighted in red; scale bars, $2 \mu\text{m}$. (C) Histograms of the probability densities for the three different mobility states of diffusing CGs on PSMs (pre-lipid-mixing state) applying different mobility filters are shown. (D) Histograms of the probability densities for the three different mobility states of diffusing CGs on PSMs (post-lipid-mixing state) applying different mobility filters are shown. To see this figure in color, go online.

structures, even though the basic setup composed of PSMs harboring the $\Delta\text{N}49$ complex is the same. Docked CGs diffuse on s-PSMs demonstrating that the formed trans-SNARE complex between synaptobrevin and SNAP25/

syntaxin 1A is mobile on the supported membranes. The support itself influences the frictional coupling of the vesicle with the planar membrane, which is, however, less pronounced compared to that of synthetic vesicles because of the large protein content in the CG membrane. The lifetimes of the docked and intermediate states of synthetic vesicles and CGs are similar, which shows that the SNARE-mediated fusion process is not greatly influenced by the vesicle membrane composition. In conclusion, our results show that the high protein content of CGs in the membrane greatly influences the first attachment of the vesicle to the planar membrane but does not alter the fusion kinetics

TABLE 1 Overview of the Fraction of CG Mobility States on PSMs

CG Mobility State ($\mu\text{m}^2/\text{s}$)	Pre-Lipid-Mixing (%)	Post-Lipid-Mixing (%)
$\text{JD} < 0.05$	33	66
$0.05 \leq \text{JD} < 0.20$	29	19
$\text{JD} \geq 0.20$	38	15

Hubrich et al.

significantly. The results further implies that even though simplistic models such as synthetic vesicles only harboring synaptobrevin 2 capture the basic features of the fusion process itself, they do not take into account any dynamics of the docked and partially fused vesicles. These findings demonstrate that only a stepwise increase in complexity will eventually lead to the full molecular picture of the fusion process in *in vitro* systems.

SUPPORTING MATERIAL

Supporting Materials and Methods, seven figures, and five videos are available at [http://www.biophysj.org/biophysj/supplemental/S0006-3495\(18\)34461-8](http://www.biophysj.org/biophysj/supplemental/S0006-3495(18)34461-8).

AUTHOR CONTRIBUTIONS

R.H. and Y.P. performed the experiments. R.H. and I.M. analyzed the data. R.J. and C.S. designed the experiments and wrote the manuscript.

ACKNOWLEDGMENTS

The authors thank the Deutsche Forschungsgemeinschaft for financial support (SFB 803, project B04).

REFERENCES

- Jahn, R., and R. H. Scheller. 2006. SNAREs—engines for membrane fusion. *Nat. Rev. Mol. Cell Biol.* 7:631–643.
- Jahn, R., T. Lang, and T. C. Südhof. 2003. Membrane fusion. *Cell.* 112:519–533.
- Aunis, D. 1998. Exocytosis in chromaffin cells of the adrenal medulla. *Int. Rev. Cytol.* 181:213–320.
- Witkowska, A., and R. Jahn. 2017. Rapid SNARE-mediated fusion of liposomes and chromaffin granules with giant unilamellar vesicles. *Biophys. J.* 113:1251–1259.
- Apps, D. K. 1997. Membrane and soluble proteins of adrenal chromaffin granules. *Semin. Cell Dev. Biol.* 8:121–131.
- Kreutzberger, A. J. B., V. Kiessling, ..., L. K. Tamm. 2017. Reconstitution of calcium-mediated exocytosis of dense-core vesicles. *Sci. Adv.* 3:e1603208.
- Park, Y., J. M. Hernandez, ..., R. Jahn. 2012. Controlling synaptotagmin activity by electrostatic screening. *Nat. Struct. Mol. Biol.* 19:991–997.
- Karatekin, E., J. Di Giovanni, ..., J. E. Rothman. 2010. A fast, single-vesicle fusion assay mimics physiological SNARE requirements. *Proc. Natl. Acad. Sci. USA.* 107:3517–3521.
- Fix, M., T. J. Melia, ..., S. M. Simon. 2004. Imaging single membrane fusion events mediated by SNARE proteins. *Proc. Natl. Acad. Sci. USA.* 101:7311–7316.
- Domanska, M. K., V. Kiessling, ..., L. K. Tamm. 2009. Single vesicle millisecond fusion kinetics reveals number of SNARE complexes optimal for fast SNARE-mediated membrane fusion. *J. Biol. Chem.* 284:32158–32166.
- Smith, E. A., and J. C. Weisshaar. 2011. Docking, not fusion, as the rate-limiting step in a SNARE-driven vesicle fusion assay. *Biophys. J.* 100:2141–2150.
- Kiessling, V., S. Ahmed, ..., L. K. Tamm. 2013. Rapid fusion of synaptic vesicles with reconstituted target SNARE membranes. *Biophys. J.* 104:1950–1958.
- Kreutzberger, A. J., V. Kiessling, and L. K. Tamm. 2015. High cholesterol obviates a prolonged hemifusion intermediate in fast SNARE-mediated membrane fusion. *Biophys. J.* 109:319–329.
- Bowen, M. E., K. Weninger, ..., S. Chu. 2004. Single molecule observation of liposome-bilayer fusion thermally induced by soluble N-ethyl maleimide sensitive-factor attachment protein receptors (SNAREs). *Biophys. J.* 87:3569–3584.
- Wang, T., E. A. Smith, ..., J. C. Weisshaar. 2009. Lipid mixing and content release in single-vesicle, SNARE-driven fusion assay with 1-5 ms resolution. *Biophys. J.* 96:4122–4131.
- Diao, J., Z. Su, ..., T. Ha. 2010. A single-vesicle content mixing assay for SNARE-mediated membrane fusion. *Nat. Commun.* 1:54.
- Kyoung, M., Y. Zhang, ..., A. T. Brunger. 2013. Studying calcium-triggered vesicle fusion in a single vesicle-vesicle content and lipid-mixing system. *Nat. Protoc.* 8:1–16.
- Lai, Y., J. Diao, ..., A. T. Brunger. 2014. Complexin inhibits spontaneous release and synchronizes Ca²⁺-triggered synaptic vesicle fusion by distinct mechanisms. *eLife.* 3:e03756.
- Yoon, T. Y., B. Okumus, ..., T. Ha. 2006. Multiple intermediates in SNARE-induced membrane fusion. *Proc. Natl. Acad. Sci. USA.* 103:19731–19736.
- Kiessling, V., A. J. B. Kreutzberger, ..., L. K. Tamm. 2018. A molecular mechanism for calcium-mediated synaptotagmin-triggered exocytosis. *Nat. Struct. Mol. Biol.* 25:911–917.
- Steyer, J. A., and W. Almers. 1999. Tracking single secretory granules in live chromaffin cells by evanescent-field fluorescence microscopy. *Biophys. J.* 76:2262–2271.
- Oheim, M., and W. Stühmer. 2000. Tracking chromaffin granules on their way through the actin cortex. *Eur. Biophys. J.* 29:67–89.
- Allersma, M. W., M. A. Bittner, ..., R. W. Holz. 2006. Motion matters: secretory granule motion adjacent to the plasma membrane and exocytosis. *Mol. Biol. Cell.* 17:2424–2438.
- Huet, S., E. Karatekin, ..., J. P. Henry. 2006. Analysis of transient behavior in complex trajectories: application to secretory vesicle dynamics. *Biophys. J.* 91:3542–3559.
- Nofal, S., U. Becherer, ..., J. Rettig. 2007. Primed vesicles can be distinguished from docked vesicles by analyzing their mobility. *J. Neurosci.* 27:1386–1395.
- Zhao, W. D., E. Hamid, ..., L. G. Wu. 2016. Hemi-fused structure mediates and controls fusion and fission in live cells. *Nature.* 534:548–552.
- Chiang, H. C., W. Shin, ..., L. G. Wu. 2014. Post-fusion structural changes and their roles in exocytosis and endocytosis of dense-core vesicles. *Nat. Commun.* 5:3356.
- Kocun, M., T. D. Lazzara, ..., A. Janshoff. 2011. Preparation of solvent-free, pore-spanning lipid bilayers: modeling the low tension of plasma membranes. *Langmuir.* 27:7672–7680.
- Schütte, O. M., I. Mey, ..., C. Steinem. 2017. Size and mobility of lipid domains tuned by geometrical constraints. *Proc. Natl. Acad. Sci. USA.* 114:E6064–E6071.
- Kuhlmann, J. W., M. Junius, ..., C. Steinem. 2017. SNARE-mediated single-vesicle fusion events with supported and freestanding lipid membranes. *Biophys. J.* 112:2348–2356.
- Schwenen, L. L., R. Hubrich, ..., C. Steinem. 2015. Resolving single membrane fusion events on planar pore-spanning membranes. *Sci. Rep.* 5:12006.
- Pobbati, A. V., A. Stein, and D. Fasshauer. 2006. N- to C-terminal SNARE complex assembly promotes rapid membrane fusion. *Science.* 313:673–676.
- Stein, S. C., and J. Thiart. 2016. TrackNTrace: a simple and extendable open-source framework for developing single-molecule localization and tracking algorithms. *Sci. Rep.* 6:37947.
- Höhne-Zell, B., A. Ecker, ..., M. Gratzl. 1994. Synaptobrevin cleavage by the tetanus toxin light chain is linked to the inhibition of exocytosis in chromaffin cells. *FEBS Lett.* 355:131–134.

35. Gersten, J., and A. Nitzan. 1981. Spectroscopic properties of molecules interacting with small dielectric particles. *J. Chem. Phys.* 75:1139–1152.
36. Dulkeith, E., A. C. Morteani, ..., D. I. Gittins. 2002. Fluorescence quenching of dye molecules near gold nanoparticles: radiative and non-radiative effects. *Phys. Rev. Lett.* 89:203002.
37. Chen, C., L. Zhang, ..., H. Zeng. 2017. Size and distance dependent fluorescence enhancement of nanoporous gold. *Opt. Express.* 25:9901–9910.
38. Schneider, G., G. Decher, ..., M. Blanchard-Desce. 2006. Distance-dependent fluorescence quenching on gold nanoparticles ensheathed with layer-by-layer assembled polyelectrolytes. *Nano Lett.* 6:530–536.
39. Anger, P., P. Bharadwaj, and L. Novotny. 2006. Enhancement and quenching of single-molecule fluorescence. *Phys. Rev. Lett.* 96:113002.
40. Floyd, D. L., S. C. Harrison, and A. M. van Oijen. 2010. Analysis of kinetic intermediates in single-particle dwell-time distributions. *Biophys. J.* 99:360–366.
41. Floyd, D. L., J. R. Ragains, ..., A. M. van Oijen. 2008. Single-particle kinetics of influenza virus membrane fusion. *Proc. Natl. Acad. Sci. USA.* 105:15382–15387.
42. Yoshina-Ishii, C., Y. H. Chan, ..., S. G. Boxer. 2006. Diffusive dynamics of vesicles tethered to a fluid supported bilayer by single-particle tracking. *Langmuir.* 22:5682–5689.
43. Kreuzberger, A. J. B., V. Kiessling, ..., L. K. Tamm. 2017. Asymmetric phosphatidylethanolamine distribution controls fusion pore lifetime and probability. *Biophys. J.* 113:1912–1915.
44. López, I., J. A. Ortiz, ..., L. M. Gutiérrez. 2009. Vesicle motion and fusion are altered in chromaffin cells with increased SNARE cluster dynamics. *Traffic.* 10:172–185.
45. Berberian, K., A. J. Torres, ..., M. Lindau. 2009. F-actin and myosin II accelerate catecholamine release from chromaffin granules. *J. Neurosci.* 29:863–870.
46. Böcker, M., S. Muschter, ..., T. E. Schäffer. 2009. Imaging and patterning of pore-suspending membranes with scanning ion conductance microscopy. *Langmuir.* 25:3022–3028.

Biophysical Journal, Volume 116

Supplemental Information

**SNARE-Mediated Fusion of Single Chromaffin Granules with Pore-
Spanning Membranes**

Raphael Hubrich, Yongsoo Park, Ingo Mey, Reinhard Jahn, and Claudia Steinem

Supporting Information

SNARE-mediated fusion of single chromaffin granules with pore-spanning membranes

Raphael Hubrich¹, Yongsoo Park^{2,3}, Ingo P. Mey¹, Reinhard Jahn² and Claudia Steinem^{1,4*}

¹Institute of Organic and Biomolecular Chemistry, University of Göttingen, Tammannstr. 2, 37077 Göttingen, Germany; ²Max-Planck-Institute for Biophysical Chemistry, Am Fassberg 11, 37077 Göttingen, Germany; ³Department of Molecular Biology and Genetics, Koc University, Rumelifeneri Yolu 34450 Sariyer, Istanbul, Turkey. ⁴Max-Planck Institute for Dynamics and Self-Organization, Am Fassberg 11, 37077 Göttingen, Germany

1. Specificity of CG docking and fusion
2. Fusion of synthetic vesicles with PSMs
3. Diffusion analysis of synthetic vesicles and CGs on PSMs
4. Localizations of CGs on PSMs
5. Displacement filter to analyze CG mobility states
6. Probability density calculations of CG localizations

1. Specificity of CG docking and fusion

Movies S1A and B (zoom in of A) show typical fusion events of CGs labeled with DiD-C₁₈ with a PSM composed of DOPC/POPE/POPS/cholesterol/PIP₂/Atto488-DPPE (48:19:10:20:2:1) and doped with the Δ N49 complex (p/l 1:500). The frame rate is 30 frames/s with scale bars of 5 μ m.

The specificity of the events of CG docking and fusion on PSMs was proven by a control experiment, in which PSMs were prepared by spreading GUVs doped with blocked Δ N49 complex. Blocking was achieved by incubation of the Δ N49 complex with the soluble SNARE domain of synaptobrevin 2 (aa 1–96) prior to reconstitution. In the recorded time series neither docking nor fusion was observed (Fig. S1, Movie S2).

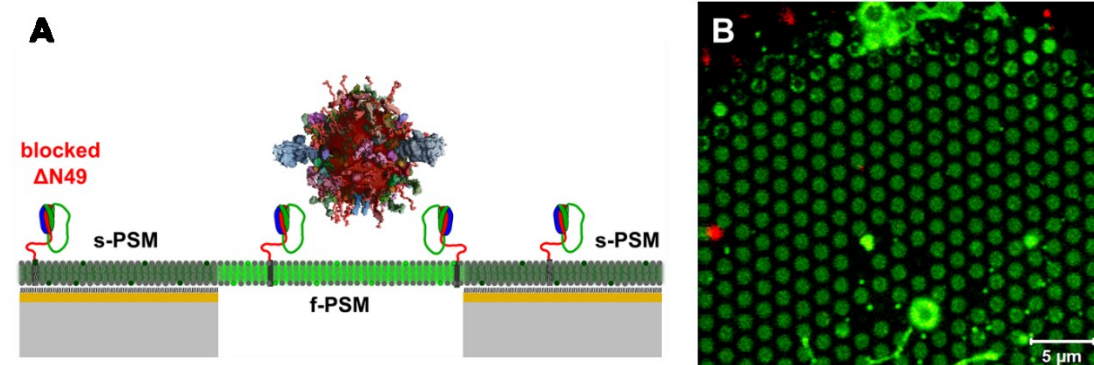


FIGURE S1 (A) Schematic illustration of the control experiment adding CGs to PSMs with blocked Δ N49 complex. (B) Snapshot of the control experiment (see Movie S2, 30 frames/s) showing CGs approaching the plane of the PSM. While no docking of CGs to the area covered by the PSM was monitored, non-specific adhesion to the membrane-uncovered surface was observed.

2. Fusion of synthetic vesicles with PSMs

For comparison, we performed a set of experiments, where we replaced labeled CGs by synthetic vesicles composed of DOPC/POPE/POPS/cholesterol/TexasRed-DPPE (50:19:10:20:1) and doped with synaptobrevin 2 (p/l 1:500). For the PSMs an identical lipid composition (DOPC/POPE/POPS/PIP₂/cholesterol/Atto488-DPPE, 48:19:10:2:20:1, doped with the ΔN49 complex (p/l 1:500) was used as for the CG fusion experiments. We evaluated 994 single fusion events to gather information about the fusion efficiency (Fig. S2A)

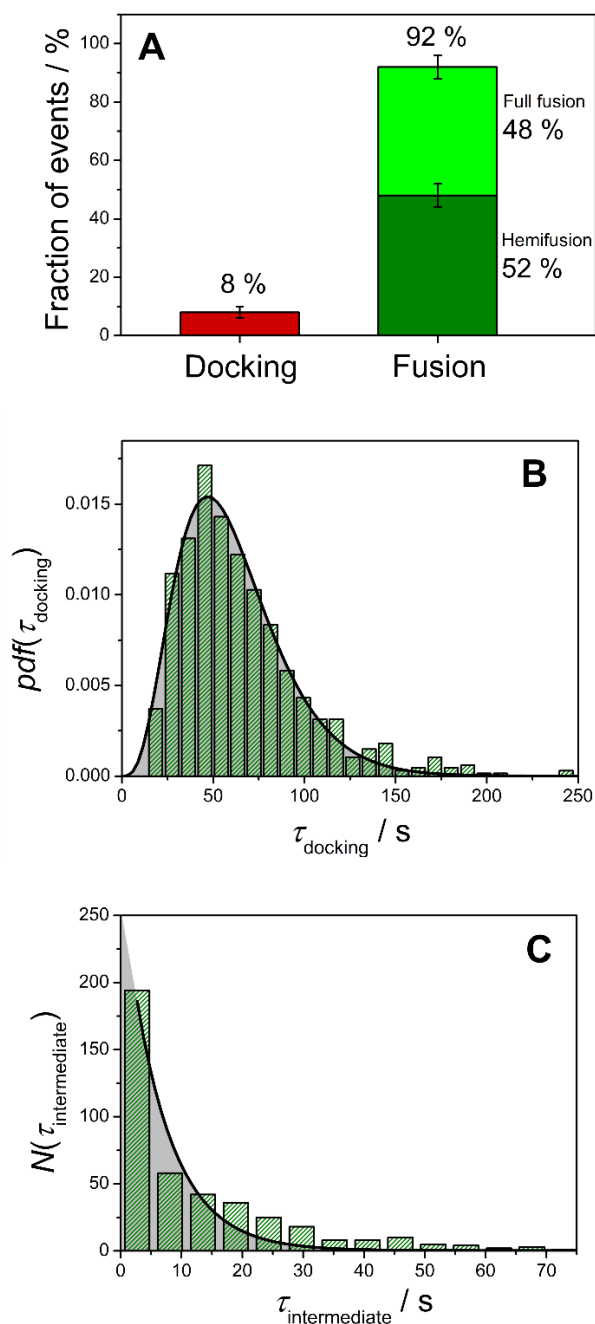


FIGURE S2 Statistical analysis of the fusion process of large unilamellar vesicles composed of DOPC/POPE/POPS/cholesterol/TexasRed-DPPE (50:19:10:20:1) and doped with synaptobrevin 2 (p/l 1:500) with PSMs composed of DOPC/POPE/POPS/PIP₂/cholesterol/Atto488-DPPE (48:19:10:2:20:1) and doped with the ΔN49 complex (p/l 1:500). (A) Fusion efficiency ($n = 994$). (B) Histogram of lifetimes of the docking state τ_{docking} ($n = 769$). The black line is the result of fitting eq. 1 to the data with $k_1 = 0.074 \pm 0.003 \text{ s}^{-1}$ and $N = 4.5 \pm 0.2$ resulting in an average docking lifetime of $\bar{\tau}_{\text{docking}} = 61 \pm 5 \text{ s}$. (C) Histogram of the lifetimes of the intermediate states $\tau_{\text{intermediate}}$ ($n = 425$). Fitting eq. 2 to the data results in a rate constant of $k_2 = 0.15 \pm 0.02 \text{ s}^{-1}$.

3. Diffusion analysis of synthetic vesicles and CGs on PSMs

Diffusion coefficients of SNARE-bound particles on the distinct parts of the PSM (f- and s-PSM) were determined by tracking the particles followed by computing the MSD from the resulting trajectories (Figs. S3 and S4). We compared the diffusive behavior of CGs on PSMs with that of synthetic vesicles composed of DOPC/POPE/POPS/cholesterol/TexasRed-DPPE (50:19:10:20:1) and doped with synaptobrevin 2 (p/l 1:500) (Fig. S3).

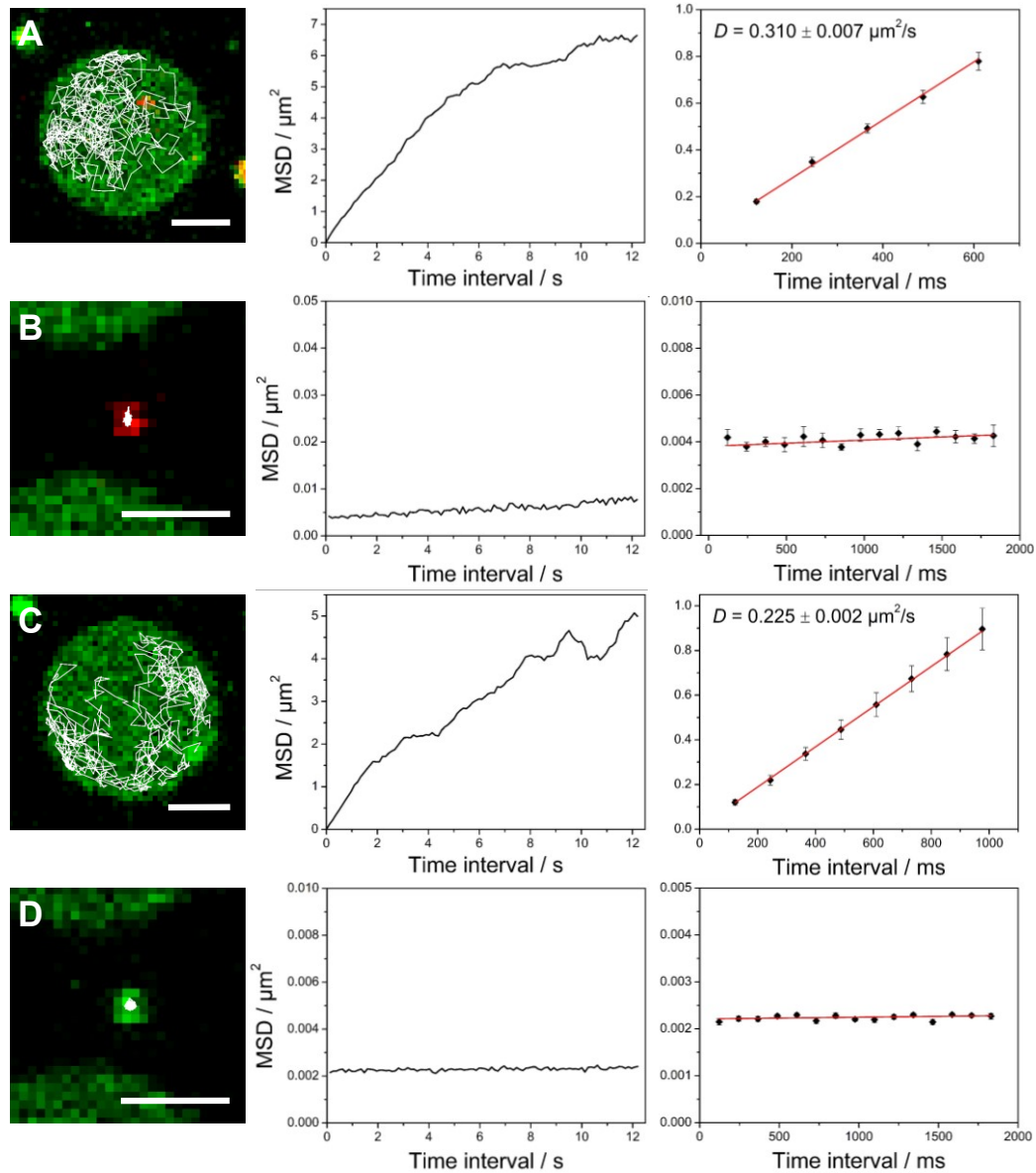


FIGURE S3 (Left) Fluorescence micrographs of synthetic vesicles composed of DOPC/POPE/POPS/cholesterol/TexasRed-DPPE (50:19:10:20:1) and doped with synaptobrevin 2 (p/l 1:500) with PSMs composed of DOPC/POPE/POPS/PIP₂/cholesterol/Atto488-DPPE (48:19:10:2:20:1) and doped with the ΔN49 complex (p/l 1:500). (A/B) before and (C/D) after the onset of lipid mixing together with the corresponding trajectories (white lines) obtained by single particle tracking. For both cases, pre- and post-lipid-mixing, an exemplary diffusion trajectory on the (A/C) f-PSM and (B/D) s-PSM is depicted; scale bars: 2 μm. (Middle) Plots of the respective, computed MSD against time intervals of up to 12 s. (Right) Diffusion coefficients D were obtained from the slope ($4D$) of MSD vs. time interval plots on shorter time scales.

Movies S3 and S4 show trajectories of CGs labeled with DiD-C₁₈ before (Movie S3) and after (Movie S4) lipid mixing with a PSM composed of DOPC/POPE/POPS/cholesterol/PIP₂/Atto488-DPPE (48:19:10:20:2:1) and doped with the ΔN49 complex (p/l 1:500). The frame rate is 30 frames/s. Fig. S4 shows representative trajectories and the corresponding MSDs.

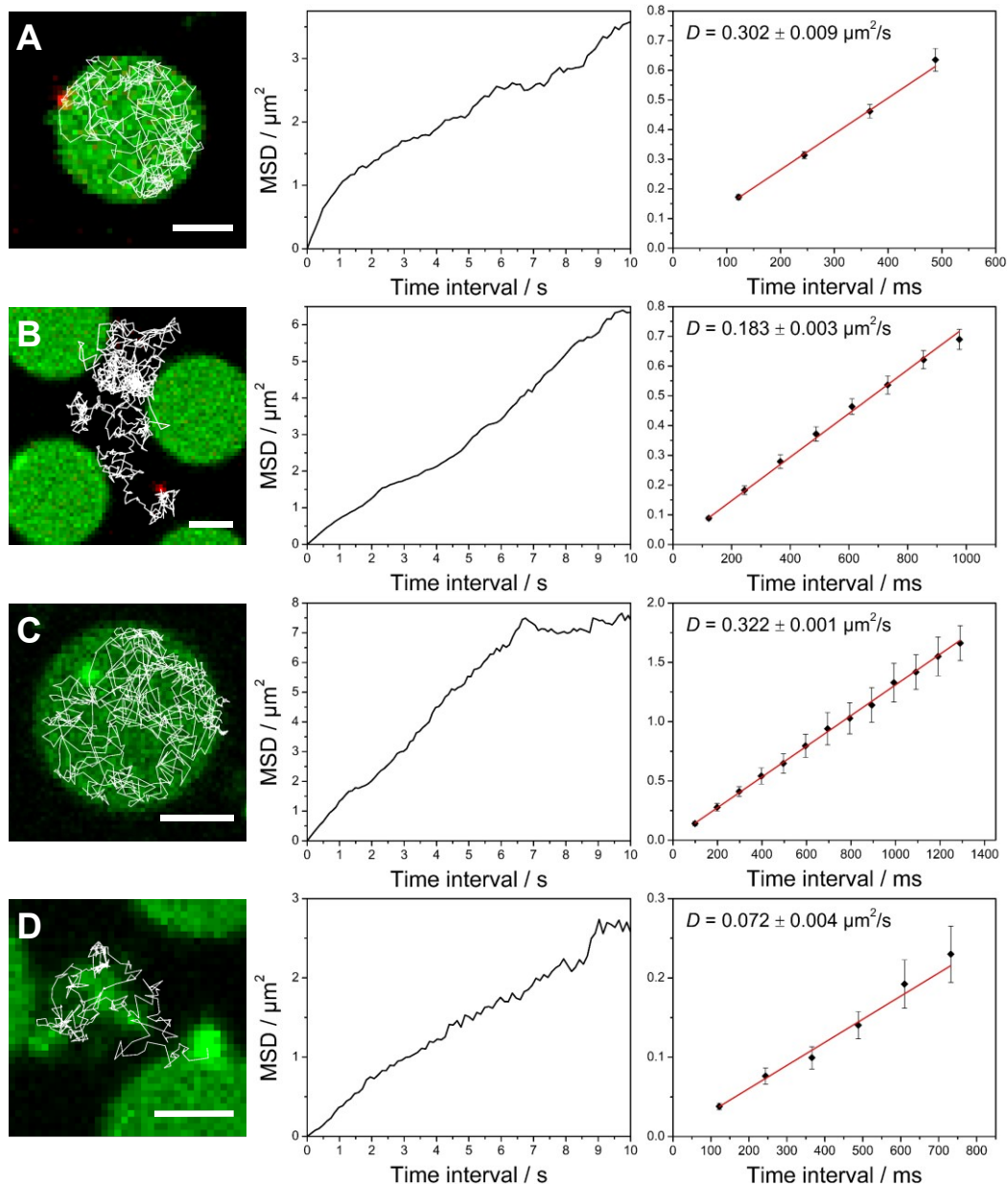


FIGURE S4 (Left) Fluorescence micrographs of mobile CGs on PSMs composed of DOPC/POPE/POPS/PIP₂/cholesterol/Atto488-DPPE (48:19:10:2:20:1) and doped with the Δ N49 complex (p/l 1:500) (A/B) before and (C/D) after the onset of lipid mixing together with the corresponding trajectories (white lines) obtained by single particle tracking. For both cases, pre- and post-lipid-mixing, an exemplary diffusion trajectory on the (A/C) f-PSM and (B/D) s-PSM is depicted; scale bars: 2 μ m. (Middle) Plots of the respective, computed MSD against time intervals of up to 10 s. (Right) Diffusion coefficients D were obtained from the slope (4D) of MSD vs. time interval plots on shorter time scales.

4. Localizations of CGs on PSMs

For pre-lipid-mixing CG diffusion, 218 diffusion trajectories from 8 different time series were evaluated. In case of post-lipid-mixing CG diffusion, 45 trajectories from 9 different time series were analyzed. The histograms (Fig. S5) show the number of detected positions as a function on the PSMs.

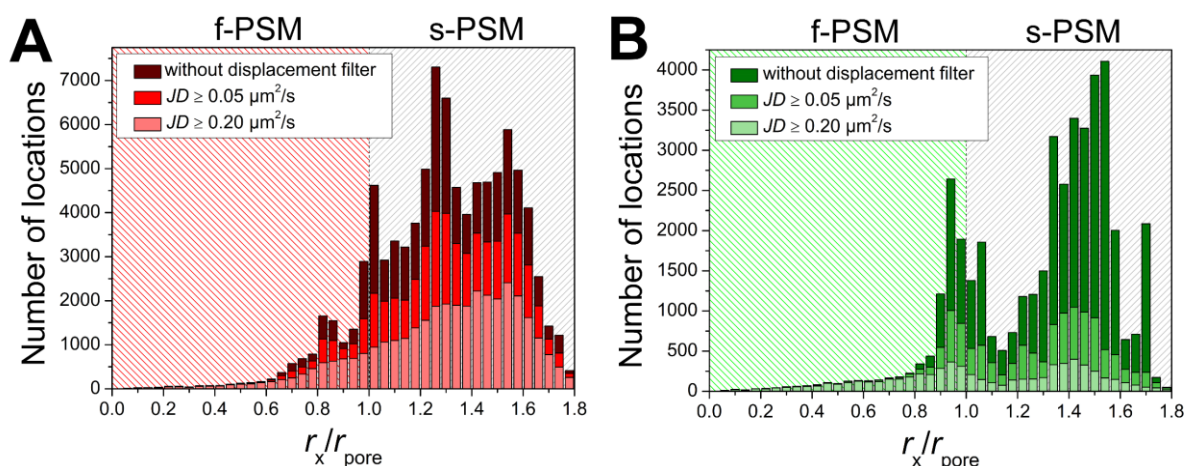


FIGURE S5 Histograms of relative pore center distances of diffusing CGs on PSMs. (A) Pore center distances of pre-lipid-mixing CG diffusion. The dark red bars display all determined CG-pore center distances, whereas the red and light red bars represent pore center distances of CGs with a jumping distance (JD) $\geq 0.05 \mu\text{m}^2/\text{s}$ and $JD \geq 0.20 \mu\text{m}^2/\text{s}$, respectively. (B) Pore center distances of post-lipid-mixing CG diffusion. The dark green bars display all determined CG-pore center distances, whereas the green and the light green bars represent pore center distances of CGs with $JD \geq 0.05 \mu\text{m}^2/\text{s}$ and $\geq 0.20 \mu\text{m}^2/\text{s}$, respectively.

5. Displacement filter to analyze CG mobility states

To have a closer look at CGs exhibiting a certain mobility state, two different displacement filters were applied. Two thresholds for the displacement of the CG's center of mass of 78 nm/122 ms and 156 nm/122 ms were set resulting in jumping distances of $0.05 \mu\text{m}^2/\text{s}$ and $0.20 \mu\text{m}^2/\text{s}$, respectively.

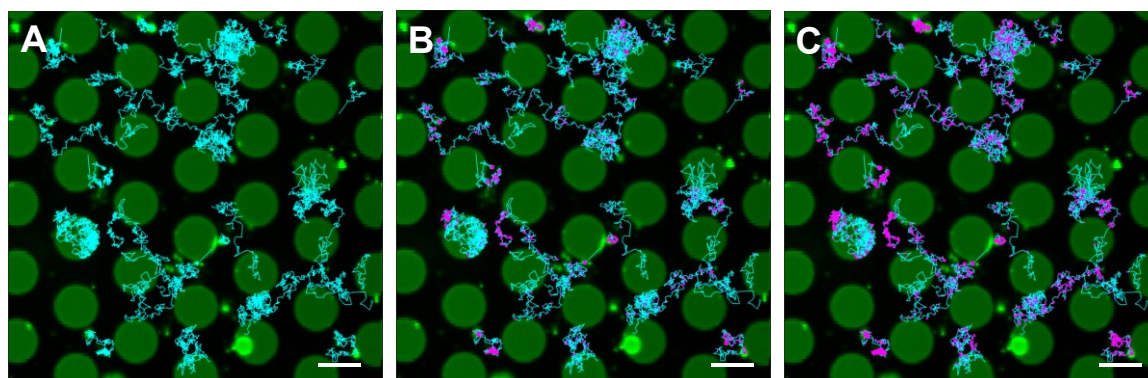


FIGURE S6 Illustration of CG diffusion trajectories before lipid mixing on PSMs (A) without a displacement filter and with a displacement filter excluding all CG locations either with a jumping distance (B) $JD < 0.05 \mu\text{m}^2/\text{s}$ or (C) $JD < 0.20 \mu\text{m}^2/\text{s}$. The PSMs are shown in green, the trajectories in turquoise and the excluded CG locations in magenta. Scale bars: $5 \mu\text{m}$.

6. Probability density calculations of CG localizations

To calculate the probability density of positions of mobile CGs on the different parts of the PSM, the binned counts with a binning of $\Delta r_x = 0.1 \mu\text{m}$ at position r_x were divided by the corresponding area segment A_x (Fig. S7).

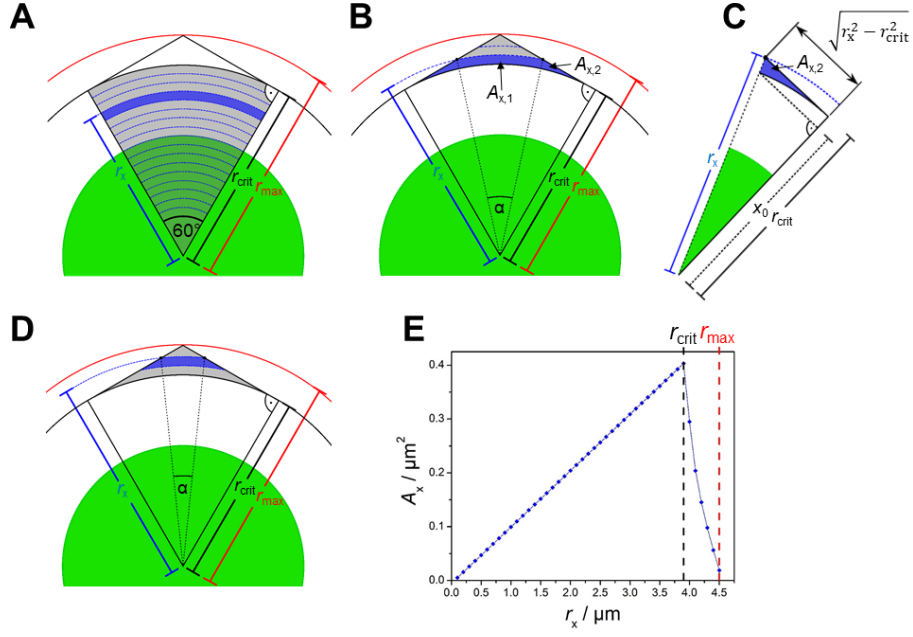


FIGURE S7 Schematic illustration to provide guidance for the derivation of the calculation of A_x . (A) Calculation of A_x as a function of r_x for $0.1 \mu m \leq r_x \leq r_{crit}$. (B-D) Calculation of A_x as a function of r_x for $r_{crit} < r_x \leq r_{max}$. (E) Plot of A_x as a function of r_x . For the given pore geometry $r_{crit} = 3.9 \mu m$ and $r_{max} = 4.5 \mu m$.

For $0.1 \mu m \leq r_x \leq r_{crit}$ with $r_x = 0$ in the pore center, the area segments with an angle of 60° are calculated according to eq. S1 (Fig. S7A):

$$A_x(r_x) = \frac{1}{6} (\pi r_x^2 - \pi (r_x - \Delta r_x)^2) \quad (S1)$$

For $4.0 \mu m \leq r_x \leq r_{max}$ the circular segments of the three pores (see Fig. 7A) start to overlap and thus a non-centrosymmetric situation arises (Fig. S7B-D). The segment area is divided into two parts $A_{x,1}$ and $A_{x,2}$ (Fig. S7B). $A_{x,1}$ is given by eq. S2:

$$A_{x,1}(r_x) = \pi (r_x^2 - r_{crit}^2) \frac{\frac{\pi}{3} - 2 \arccos\left(\frac{r_{crit}}{r_x}\right)}{2\pi} \quad (S2)$$

$A_{x,2}$ is given by the following integral (eq. S3):

$$A_{x,2}(r_x) = \int_{x_0}^{r_{crit}} \frac{\sqrt{r_x^2 - r_{crit}^2}}{r_{crit}} x - \sqrt{r_{crit}^2 - x^2} dx \quad (S3)$$

with $x_0 = r_{crit}^2 / r_x$. For $r_x = 4.0 \mu m$, $A_x(r_x) = A_{x,1}(r_x) + 2 A_{x,2}(r_x)$, for $r_x > 4.0 \mu m$, $A_x(r_x) = A_{x,1}(r_x) - A_{x,1}(r_x - \Delta r_x) + 2 (A_{x,2}(r_x) - A_{x,2}(r_x - \Delta r_x))$. Fig. S7E shows the result of the area segments A_x as a function of r_x .

By applying the displacement filter to the monitored CG diffusion trajectories, the normalized counts of r_x as well as the corresponding probability densities were determined for the three different mobility states of CG diffusion.